A Threshold Voltage Model of Silicon-Nanotube-Based Ultrathin Double Gate-All-Around (DGAA) MOSFETs Incorporating Quantum Confinement Effects

Arun Kumar, Shiv Bhushan, and Pramod Kumar Tiwari, *Member, IEEE*

***Abstract*—In this paper, a quantum-mechanical threshold voltage model for ultrathin double gate-all-around DGAA MOSFETs has been developed by solving three-dimensional (3-D) Poisson's and 2-D Schrödinger's equations in the channel region. The parabolic potential approximation is considered for Poisson's equation solution, whereas a hollow cylindrical potential well in the channel region is assumed to solve Schrödinger's equation. Simple equations for the wave function and energy quantization in the channel of DGAA MOSFET have been formulated. Discretized energy levels have been used for channel charge calculation in subthreshold regime of device operation. The calculated channel charge is compared with a threshold charge to formulate the threshold voltage model. The effects of the device parameters such as the channel thickness, oxide thickness, doping, etc. on threshold voltage and DIBL have been extensively studied. The proposed model results have been verified by comparing with the numerical simulation results obtained from the 3-D device simulator Visual TCAD of Cogenda Int.**

***Index Terms*—DGAA MOSFET, quantum confinement, electric field, inversion charge density, threshold voltage, DIBL.**

I. Introduction

SUB-30 nm metal-oxide-semiconductor field-effect-transistor (MOSFET) scaling demands not only new materials and technologies but also innovative non-conventional geometrical structures [1]–[3]. A number of innovative MOSFET structures, from silicon-on-insulator (SOI) to gate-all-around (GAA), have been rigorously analyzed to further increase the scaling limit and find their suitability for ultra-large-scale integration (ULSI). The SOI MOSFET adopts an innovative silicon-on-insulator substrate to improve the device performance, whereas, a unique circular gate wrapped around a vertical cylindrical silicon nanowire makes the GAA MOSFETs [4], [5]. A nanowire based GAA MOSFET, although, seems to have excellent short-channel- effects immunity [5], [6], a number of technological issues including large contact area requirement and large series resistance limit its utility for ULSI [3]. Moreover, the on-current delivered by the device is also quite low [7]. Recently, a novel device namely double gate-all-around (DGAA) MOSFET or silicon-nano-tube (Si-NT) FET, which may be a potential candidate for future ULSI, is proposed, fabricated and tested [8], [9]. The proposed structure utilizes a tubular Si-channel which remains surrounded by cylindrical shell (outer) and core (inner) gates. The presence of two gates gives rise to ultimate short-channel effects immunity and volume inversion and, therefore, the device has excellent OFF- and ON- state electrical characteristics [8], [10].

To obtain the first hand information about the threshold voltage of DGAA MOSFET, a threshold voltage model was presented in our previous work [11]. However, the model [11] was not suitable for an ultra-scaled device as quantum confinement effects were not incorporated. When the effective channel length of a device is scaled down to 20 nm or less, an ultrathin channel is required to cut down the short-channel effects. However, the ultrathin channel also gives rise to the quantum mechanical effects.

In ultra-scaled devices, the distribution and transport properties of the carriers are quite different from the classical case as the motion of carriers are confined due to ultra-scaled device dimension leading to shift in threshold voltage, tunneling current etc. thus, these effects need to be incorporated in an analytical model of DGAA MOSFET for accurately investigating its subthreshold characteristics.

In this work, a threshold voltage model is reported for ultrathin DGAA MOSFETs considering the quantum confinement effects. The present model considers a hollow cylindrical potential well in the channel region to determine the wave-function and discrete energy levels. The inversion charge concentration is determined using these discrete energy levels. The threshold voltage is formulated by comparing the inversion charge with a critical charge which is determined from numerical simulations. The model results are compared with the numerical simulation results.

Manuscript received February 25, 2017; revised June 8, 2017; accepted June 13, 2017. Date of publication June 22, 2017; date of current version September 6, 2017. This work was supported in part by the Defence Research and Development Organization, Ministry of Defence, Government of India under Grant ERIP/ER/1506039/M/01/1589 and in part by the Council of Scientific and Industrial Research, Government of India under Grant 09/1023(0016)/2016-EMR-I. The review of this paper was arranged by Associate Editor F. Ye. *(Corresponding author: Pramod Kumar Tiwari.)*

The authors are with the Department of Electrical Engineering, Indian Institute of Technology Patna, Patna 801103, India (e-mail: arun.pee16@iitp.ac.in; shivbhushan1510@gmail.com; pktiwari@iitp.ac.in).

Color versions of one or more of the figures in this paper are available online at http://ieeexplore.ieee.org

Digital Object Identifier 10.1109/TNANO.2017.2717841

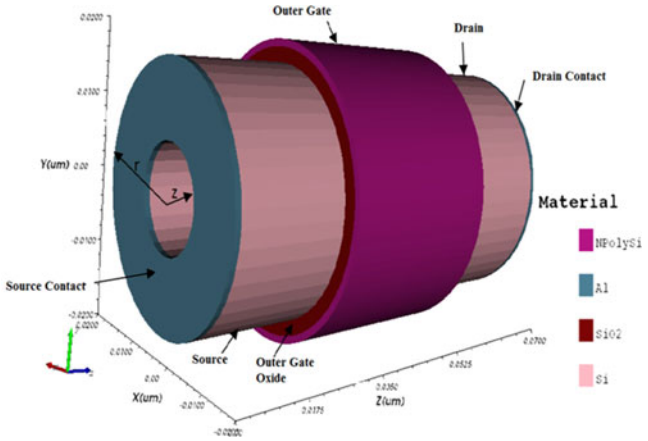

Fig. 1. 3D simulated structure of DGAA MOSFET.

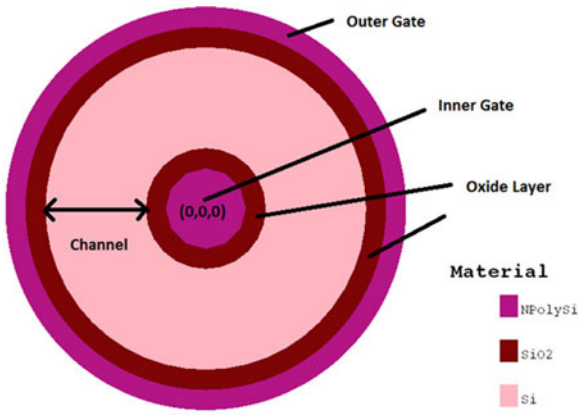

Fig. 2. Circular cross section view of DGAA MOSFET.

II. Device Structure

Three-dimensional (3D) view of a cylindrical DGAA MOSFETs having tubular channel controlled by inner and outer gates is shown in Fig. 1. The inner gate surrounded by oxide layer support enhanced charge control in channel region while the outer gate is similar to GAA. The circular cross-section view with origin at the center of the tube towards the source end is shown in Fig. 2. The 2-D cross-sectional view is shown in Fig. 3 depicting the different device regions.The radial and lateral directions of cylindrical coordinate system are assumed to be along the radius and the length of the cylindrical channel. The device has uniformly doped source and drain with doping density of $N_{\rm d} = 10^{20}$ cm^{-3}. The channel is kept lightly doped with doping density of $N_{\rm a} = 10^{15}$ cm^{-3}. The gate oxide thickness, inner gate radius and channel thickness (tube thickness) are noted as $t_{\rm ox}$, $t_{\rm c}$ and $t_{\rm si}$ respectively. The device is symmetrical with both inner and outer gates having same voltage biasing $V_{\rm G}$ and work function $\varphi_{\rm m} = 4.7$ eV. The standard value of permittivity is considered for both silicon and SiO_2 as $\epsilon_{\rm si} = 11.8 \times 8.854 \times 10^{-14}$F/cm and $\epsilon_{\rm ox} = 3.97 \times 8.854 \times 10^{-14}$F/cm respectively. In this work, the Si nanotube is considered to be oriented along the <100> silicon lattice direction.

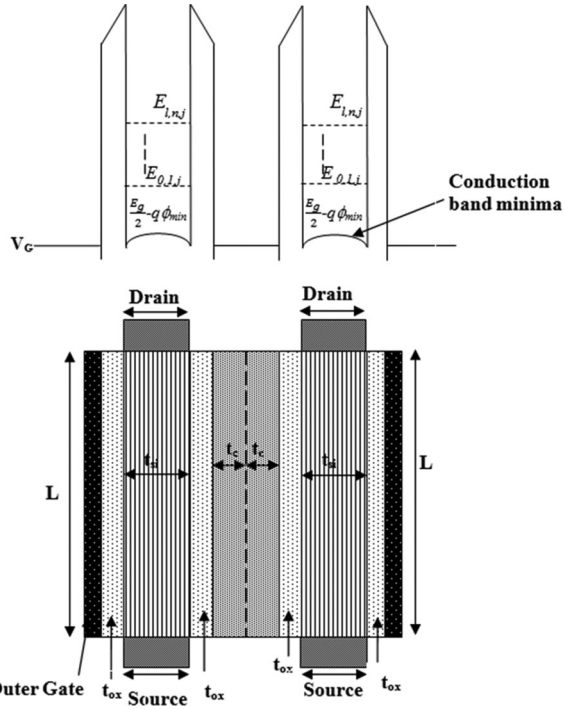

Fig. 3. 2-D Cross sectional view of a double gate-all-around (DGAA) MOSFET with discrete energy levels in channel.

III. Modeling

In ultra-scaled DGAA MOSFETs, the quantization of electronic energy in ultra-thin channel region due to structural confinement becomes significant. Therefore, the Poisson-Schrödinger equation should be solved in a coupled manner to determine channel potential distribution $\phi(r, \theta, z)$ and inversion charge density, $Q_{\rm inv}$. However, the self-consistent approach to solve the coupled equations does not provide analytical expressions for potential and charge distribution. Further, sophisticated computer programs are required to run for longer time period to determine the charge density.

In the subthreshold regime of device operation, the inversion charge concentration is not very significant compared to the impurity concentration, and therefore, the mobile carriers cannot effectively screen the channel electrostatics potential [6], [12]. Therefore, the electrostatic channel potential could be determined by solving Poisson's equation while neglecting the mobile charge term. Neglecting the effect of mobile charges on channel electrostatics potential in turn facilitates the decoupling of Poisson's and Schrödinger's equations. The decoupled Poisson's and Schrödinger's equation can be written in the cylindrical co-ordinate system as follows:

$$\frac{1}{r}\frac{d}{dr}\left[r\frac{d}{dr}\phi(r,\theta,z)\right] + \frac{1}{r^2}\frac{d^2}{d\theta^2}\phi(r,\theta,z) + \frac{d^2}{dz^2}\phi(r,\theta,z) = \frac{qN_{\rm a}}{\epsilon_{\rm si}} \tag{1}$$

$$-\frac{\hbar^2}{2m_{\rm e}}\left[\frac{d^2}{dr^2} + \frac{1}{r}\frac{d}{dr} + \frac{1}{r^2}\frac{d^2}{d\theta^2} + \frac{d^2}{dz^2} + U(r,\theta,z)\right]$$

$$\psi(r,\theta,z) = E\psi(r,\theta,z) \tag{2}$$

where, $\phi(r,\theta,z)$ and $\psi(r,\theta,z)$ are the electrostatic potential in the channel region and electron wave function, respectively. The electron effective mass is noted as $m_{\rm e}$, $\hbar = \frac{h}{2\pi}$ is the reduced Planck's constant, $U(r,\theta,z)$ is the potential energy of the carrier and E is discretized conduction band energy levels in the channel region.

A. Channel Potential and Electric Field Formulation

Considering the variation of potential along the angular direction is ineffective, (1) reduces to

$$\frac{1}{r}\frac{d}{dr}\left[r\frac{d}{dr}\phi\left(r,z\right)\right]+\frac{d^2}{dz^2}\phi\ \left(r,z\right)=\frac{qN_a}{\epsilon_{\rm si}} \tag{3}$$

Equation (3) may be solved by assuming following parabolic potential along radius of the DGAA MOSFET

$$\phi\ \left(r,z\right)=C_0\ \left(z\right)+C_1\left(z\right)r+C_2\left(z\right)r^2 \tag{4}$$

where, $C_0\ (z)$, $C_1\ (z)$ and $C_2(z)$ are z-dependent functions and can be determined by solving following boundary conditions

$$\frac{d}{dr}\phi\ \left(r=t_c+t_{\rm ox},z\right)=\frac{C_{ox}}{\epsilon_{si}}\ \left(\phi_1-\left(V_G\ -V_{\rm fb}\right)\right) \tag{5}$$

$$\frac{d}{dr}\phi\ \left(r=t_c+t_{\rm ox}+t_{\rm si},z\right)=\frac{C_{ox}}{\epsilon_{si}}\ \left(-\phi_2+\left(V_G\ -V_{\rm fb}\right)\right) \tag{6}$$

here, $C_{\rm ox}=\frac{\epsilon_{\rm ox}}{t_{\rm ox}}$, $\phi_1=\phi(r=t_c+t_{\rm ox},z)$ and $\phi_2=\phi(r=t_c+t_{\rm ox}+t_{\rm si},z)$ are inner and outer surface potential.

Parameter V_{fb} is flat band voltage given by

$$V_{fb}=\varphi_m-\left(\chi_{\rm si}+\frac{E_g}{2q}+V_T\ln\left(\frac{N_a}{n_i}\right)\right) \tag{7}$$

where, $\chi_{\rm si}, E_g$, $V_T=\frac{KT}{q}$ and n_i are electron affinity, silicon band gap energy, thermal voltage and the standard intrinsic concentration of silicon respectively.

We have already solved (3) using (4), (5) and (6) for DGAA MOSFET in our previous work [11], the inner surface potential $\phi_1=\phi(r=t_c+t_{\rm ox},z)$ and the channel potential $\phi(r,z)$ were determined to be

$$\phi_1\left(r=t_c+t_{\rm ox},z\right)=C_3e^{\sqrt{\alpha_1}z}+C_4e^{-\sqrt{\alpha_1}z}+\sigma_1 \tag{8}$$

$$\phi\left(r,z\right)=\phi_1\left[1-\epsilon_r\left(a-br+cr^2\right)\right]+\left(V_G-V_{\rm fb}\right)\epsilon_r\left[n-pr+qr^2\right] \tag{9}$$

where, the constants are device dependent parameters as discussed in [11]. The so-called virtual cathode potential position, $(z=z_{min})$, which is the leakiest position in the channel region, was also determined by differentiating (8) and equating it to zero [11]. The virtual cathode position expression was found as

$$z_{\rm min}=\frac{ln\left(\frac{C_4}{C_3}\right)}{2\sqrt{\alpha_1}} \tag{10}$$

Utilizing (10) and (8) in (9) gives the following minimum potential at virtual cathode point

$$\phi_{\rm vc}=\phi\left(r,z=z_{\rm min}\right) \tag{11}$$

$$\phi_{\rm vc}=\left[2\sqrt{C_3C_4}+\sigma_1\right]\left[1-\epsilon_r\left(a-br+cr^2\right)\right]+\left(V_G-V_{\rm fb}\right)\epsilon_r\left[n-pr+qr^2\right] \tag{12}$$

The $r=r_{\rm min}$ point at which the channel potential reaches its maximum value is evaluated in two steps. The function $\phi(r,z=z_{\rm min})$ of (12) is differentiated with respect to $'r'$ at first and then the resulting function is equated to zero to determine

$$r_{\rm min}=\frac{b\left[2\sqrt{C_3C_4}+\sigma_1\right]-p\left(V_G-V_{\rm fb}\right)}{2c\left[2\sqrt{C_3C_4}+\sigma_1\right]-2q\left(V_G-V_{\rm fb}\right)} \tag{13}$$

Substituting the above $r_{\rm min}$ in (12) gives the maximum value of potential $\phi(r=r_{\rm min},z=z_{\rm min})$.

Further, the electric field $E_Z=-\frac{d}{dz}\phi(r,z)$ along the channel can be obtained by differentiating (9) with respect to z as

$$E_z=-\frac{\sqrt{\alpha_1}}{sinh\sqrt{\alpha_1}L}\left(1-\epsilon_r\left(a-br+cr^2\right)\right)\left[-\left(V_{bi}-\sigma_1\right)\times cosh(\sqrt{\alpha_1}\left(L-z\right)+\left(V_{ds}+V_{\rm bi}-\sigma_1\right)cosh\left(\sqrt{\alpha_1}z\right)\right] \tag{14}$$

where, $V_{\rm ds}$ and $V_{\rm bi}=V_T\ \ln(\frac{N_aN_d}{n_i^2})$ are drain voltage biasing and built-in potential respectively.

B. Wave Function and Energy Value Calculation

Now, we can simplify (2) by considering the electrons confinement only in transverse direction of the carriers' movement. Thus, (2) could be written as

$$-\frac{\hbar^2}{2m_e}\left[\frac{d^2}{dr^2}+\frac{1}{r}\frac{d}{dr}+\frac{1}{r^2}\frac{d^2}{d\theta^2}\right]\psi\left(r,\theta\right)+\left(U-E\right)\psi\left(r,\theta\right)=0 \tag{15}$$

Since, there are large potential barriers at both Si-SiO_2 interfaces, to solve (15); it may be considered that a hollow cylindrical potential well is formed in the channel region of DGAA MOSFETs with bottom represents the minima of conduction band energy at virtual cathode as shown in Fig. 3.

The $U(r,\theta)$ may be defined in terms of band-gap energy E_g and potential $\phi(r=r_{\rm min},z=z_{\rm min})$, and can be written as

$$U\left(r,\theta\right)=E_O=\frac{E_g}{2}-q\phi\left(r=r_{\rm min},z=z_{\rm min}\right) \tag{16}$$

Now, re-arranging the terms, we can re-write (15) as

$$\left[\frac{d^2}{dr^2}+\frac{1}{r}\frac{d}{dr}+\frac{1}{r^2}\frac{d^2}{d\theta^2}\right]\psi\left(r,\theta\right)+k^2\psi\left(r,\theta\right)=0 \tag{17}$$

$$\text{where, } k=\sqrt{\frac{2m_e}{\hbar^2}\left(E-U\right)} \tag{18}$$

In order to obtain the solution of (17); the separation of variables method is utilized. The solution of wave function $\psi(r,\theta)$ can be written as the product of independent functions of r and θ [13].

$$\psi\left(r,\theta\right)=R\left(r\right)\cdot\Theta\left(\theta\right) \tag{19}$$

The $\Theta(\theta)$ function is periodic due to the angular symmetry of the channel region; its solution can be given individually as [14], [15]

$$\Theta(\theta) = e^{il\theta} \tag{20}$$

with $l = 0, \pm 1, \pm 2..$ given as angular quantum number. Substituting the value of (19) into (17) and divide by $\Theta(\theta)$, (17) results into

$$\left[r^2 \frac{d^2}{dr^2} + r\frac{d}{dr}\right] R(r) + \left(k^2 - l^2\right) R(r) = 0 \tag{21}$$

Considering a hollow cylindrical potential well in the channel as discussed above, the general solution of (21) could be written as [14]

$$R(r) = RJ_l(k_{l,n}r) + SY_l(k_{l,n}r) \tag{22}$$

where, R and S are constants evaluated using normalization and boundary conditions, J_l and Y_l are Bessel functions of first and second kind with order l respectively. The Bessel function of second kind Y_l is allowed in the case of DGAA, although for a Gate all around (GAA) nanowire, it is discarded due to divergent behavior at the origin [15].

Thus, the complete wave function $\psi(r, \theta)$ could be written by substituting the values of (20) and (22) in (19) as

$$\psi(r, \theta) = \left[\left(RJ_l(k_{l,n}r) + SY_l(k_{l,n}r)\right).\left(e^{il\theta}\right)\right] \tag{23}$$

The solution of (22) with vanishing boundary condition i.e. $\psi(r, \theta) = 0$ at both inner $r_1 = r_c(1 - \frac{t_{si}}{2r_c})$ and outer $r_2 = r_c(1 + \frac{t_{si}}{2r_c})$ channel-oxide interfaces, leads to the following Bessel function equation [14].

$$J_l\left(k_{l,n}r_c\left(1 + \frac{t_{si}}{2r_c}\right)\right).Y_l\left(k_{l,n}r_c\left(1 - \frac{t_{si}}{2r_c}\right)\right) - J_l\left(k_{l,n}r_c\left(1 - \frac{t_{si}}{2r_c}\right)\right).Y_l\left(k_{l,n}r_c\left(1 + \frac{t_{si}}{2r_c}\right)\right) = 0 \tag{24}$$

where, r_c is an effective radius from the origin of the device to the mid of the channel and n is defined as radial quantum number given as $n = 1, 2, 3 \ldots$

We can now plot the $f(k_{l,n}r_c)$ from (24) and thereby determine the value of $k_{l,n}r_c$ for which

$$f(k_{l,n}r_c) = 0 \tag{25}$$

The value of $k_{l,n}r_c$ is n^{th} zero of l^{th} order of Bessel equation evaluated from Fig. 4.

The dispersion relation of E and k, which relates the energy of electronic wave function and wave vector respectively, specify the electronic structure of silicon as discussed in (18).

Moreover, each electron corresponds to six different ellipsoidal surfaces of constant energy or valleys and each valley is characterized by an effective mass of $m_l = 0.97\ m_o$ along its orientation axis and $m_t = 0.19\ m_o$ along its transverse direction where, $m_o = 9.1 \times 10^{-31}$ kg is the rest mass of electron. Considering the transport of electron from source to drain along z-axis, the confinement mass of the electron in transverse valleys is approximated as cylindrical mass $m_c = \frac{2m_l m_t}{m_l + m_t} = 0.315\ m_o$ and for longitudinal valley as $m_t = 0.19\ m_o$, respectively. This

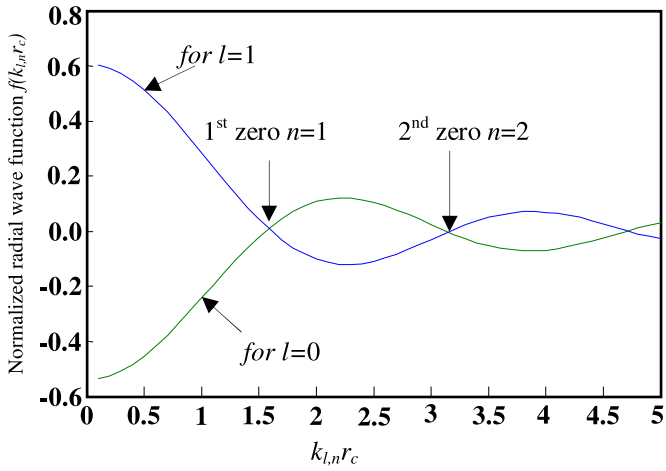

Fig. 4. Normalized wave function along radial direction.

dependence of effective mass on discrete energy levels E is accounted by the index j [16]–[18].

As the electrons are travelling from source to drain in z-direction, there will be carrier confinement in radial direction due to gate control over the channel which is orthogonal to the direction of carrier flow, hence, the quantized sub-band energy value $E^i_{l,n,j}$ in radial direction for cylindrical and longitudinal confined mass of electron is given using (25) and (18) as [5], [14]

$$E^i_{l,n,j} = E^i_{l,n,j=1,2} = \frac{(i\hbar)^2}{2{r_c}^2}\left(\frac{1}{m_c}\right)(k_{l,n}r_c)^2 \tag{26}$$

$$E^i_{l,n,j} = E^i_{l,n,j=3} = \frac{(i\hbar)^2}{2{r_c}^2}\left(\frac{1}{m_t}\right)(k_{l,n}r_c)^2 \tag{27}$$

From the above equations, we can conclude that Eigen states i.e. discrete energy level of carrier in channel region will shift in ascending order following any change in the value of quantum number l & n. In general, the total sub-band energy (Eigen values) for the $i = 1$ conduction sub-band can be given using (16), (18), (26) and (27) as

$$E^1_{l,n,j} = \frac{E_g}{2} - q\phi(r = r_{\min}, z = z_{\min}) + \frac{(\hbar)^2}{2{r_c}^2}\left(\frac{1}{m_c}\right) \times (k_{l,n}r_c)^2 + \frac{(\hbar)^2}{2{r_c}^2}\left(\frac{1}{m_t}\right)(k_{l,n}r_c)^2 \tag{28}$$

C. Inversion Charge Density Calculation

For each energy level $E^i_{l,n,j}$ referenced with respect to the minima E_o of the cylindrical potential well, the contribution to the total charge over the channel region per unit length is calculated using the theory of density of states (DOS) [19]. The inversion charge density is calculated as [17], [19]

$$Q_{\text{inv}} = q\int_{E_0}^{\infty} g(E) f(E)\, dE \tag{29}$$

Where, $$g(E) = \frac{2}{\pi}\sqrt{\frac{m_z}{2\hbar^2}}\sum_i\sum_j \frac{1}{\sqrt{E - E^i_{l,n,j}}} \tag{30}$$

$g(E)$ is the density of states of electrons in 1-D [17] and,

$$f(E) = \frac{1}{1+\exp\left(\frac{E-E_F}{KT}\right)} \tag{31}$$

is the approximated Fermi-Dirac function which defines the probability of finding electrons in particular states [19].

Substituting the values of $g(E)$ and $f(E)$ in (29) leads to

$$Q_{\text{inv}} = 2q\sum_i\sum_j \frac{1}{\pi}\sqrt{\frac{m_z}{2\hbar^2}}\int_{E_0}^{\infty}\frac{1}{\sqrt{E-E^i_{l,n,j}}} \times \frac{1}{1+\exp\left(\frac{E-E_F}{KT}\right)}dE \tag{32}$$

here, $m_z = m_l$ is the effective mass of electron orthogonal to the direction of energy quantization.Under non-degenerate condition (valid at threshold) [17] and in the weak inversion region, the Fermi level is found to be much below the conduction band energy level. So, the Fermi-Dirac distribution can be approximated by a simple exponential corresponding to Boltzmann's distribution. The expression for the inversion charge becomes [17], [20]

$$Q_{\text{inv}} = q\sum_i\sum_j \frac{1}{\pi}\sqrt{\frac{2m_z}{\hbar^2}}\sqrt{\frac{KT}{q}} \times \sqrt{\pi} \times \exp\left(\frac{-E^i_{l,n,j}}{V_T}\right) \tag{33}$$

$$Q_{\text{inv}} = q\sum_i\sum_j \sqrt{\frac{2m_z KT}{q\pi\hbar^2}}\exp\left(\frac{-E^i_{l,n,j}}{V_T}\right) \tag{34}$$

However, it is found that lowest energy level $i = 1$ contains most of the electron, it is sufficient to predict the charge density using only lowest energy level for further analysis [20]. The total inversion charge density at minima of channel $z = z_{\text{min}}$ is found to be

$$Q_{\text{inv}} = q\sqrt{\frac{2m_z KT}{q\pi\hbar^2}}\exp\left(\frac{-E_{l,n,j}}{V_T}\right) \tag{35}$$

Substituting the values of $E_{l,n,j}$ from (28) for $l = 0$ and $n = 1$ in above, we get Q_{inv} shown in (36) at the bottom of this page. Now, re-arranging the terms, we can rewrite (36) as shown at the bottom of this page,

$$\phi(r = r_{\text{min}}, z = z_{\text{min}}) = \frac{E_g}{2} + \frac{(\hbar)^2}{2{r_c}^2}\left(\frac{1}{m_c}\right)(k_{0,1}r_c)^2 + \frac{(\hbar)^2}{2{r_c}^2}\left(\frac{1}{m_t}\right)(k_{0,1}r_c)^2 + V_T \ln\left(\frac{Q_{\text{inv}}}{q\sqrt{\frac{2m_z KT}{q\pi\hbar^2}}}\right) \tag{37}$$

D. Calculation of Threshold Voltage

The threshold voltage (V_{th}) is defined as the gate voltage at which the minimum of the surface potential becomes equal to twice of the Fermi potential $\phi_{\text{vc}} = 2\phi_{\text{f}}$. However, this definition is not very accurate for undoped non-conventional MOSFETs [6]. The more accurate definition of V_{th} for non-conventional MOSFETs is defined as the gate voltage V_{G} at which the inversion charge density becomes equal to a critical (threshold) charge density $Q_{\text{inv}} = Q_{\text{th}}$. Using (12) and (37) and on equating both,

$$\frac{E_g}{2} + \frac{\hbar^2}{2{r_c}^2}\left(\frac{1}{m_c}\right)(k_{0,1}r_c)^2 + \frac{\hbar^2}{2{r_c}^2}\left(\frac{1}{m_t}\right)(k_{0,1}r_c)^2 + V_T \ln\left(\frac{Q_{\text{inv}}}{q\sqrt{\frac{2m_z V_T}{\pi\hbar^2}}}\right) = \left[2\sqrt{C_3 C_4} + \sigma_1\right]\left[1-\epsilon_r(a-br+cr^2)\right] + (V_G - V_{\text{fb}})\,\epsilon_r\left[n - pr + qr^2\right] \tag{38}$$

The following second order equation is obtained by replacing $Q_{\text{inv}} = Q_{\text{th}}$ when $V_{\text{G}} = V_{\text{th}}$ in (38)

$$\left(a_1 a_2^2 - a_4^2\right)(V_{\text{th}} - V_{\text{fb}})^2 + \left(a_1^2 a_6 + 2a_2 a_7\right)(V_{\text{th}} - V_{\text{fb}}) + \left(a_1^2 a_8 - a_7^2\right) = 0 \tag{39}$$

where,

$$a_1 = \frac{1 - \frac{\epsilon_{\text{ox}}}{\epsilon_{\text{si}} t_{\text{si}} t_{\text{ox}}}\left[(t_c + t_{\text{ox}})(2t_c + t_{\text{ox}}) - (t_{\text{si}} + 2t_c + 2t_{\text{ox}})\,r + r^2\right]}{sinh\left(\sqrt{\alpha_1}L\right)} \tag{40}$$

$$a_2 = 2\left[\frac{\frac{\epsilon_{\text{ox}}}{\epsilon_{\text{si}} t_{\text{si}} t_{\text{ox}}}\left(3 - \frac{t_c}{t_{\text{si}} + t_c + 2t_{\text{ox}}}\right)}{\alpha_1}\right]^2 . \left(cosh\left(\sqrt{\alpha_1}L\right) - 1\right) \tag{41}$$

$$a_3 = 1 - \frac{\epsilon_{\text{ox}}}{\epsilon_{\text{si}} t_{\text{si}} t_{\text{ox}}}\left[(t_c + t_{\text{ox}})(2t_c + t_{\text{ox}}) - (t_{\text{si}} + 2t_c + 2t_{\text{ox}})\,r + r^2\right] \tag{42}$$

$$a_4 = 1 + a_3\left[\frac{\frac{\epsilon_{\text{ox}}}{\epsilon_{\text{si}} t_{\text{si}} t_{\text{ox}}}\left(3 - \frac{t_c}{t_{\text{si}} + t_c + 2t_{\text{ox}}}\right)}{\alpha_1} - 1\right] \tag{43}$$

$$a_5 = \frac{\epsilon_{\text{ox}}}{\epsilon_{\text{si}} t_{\text{si}} t_{\text{ox}}}\left(3 - \frac{t_c}{t_{\text{si}} + t_c + 2t_{\text{ox}}}\right) \tag{44}$$

$$a_6 = -\left[\frac{a_5 4qN_a}{\epsilon_{\text{si}}\alpha_1^2} + \frac{2(2V_{\text{bi}} + V_{\text{ds}})\,a_5}{\alpha_1}\right] . \left(cosh\left(\sqrt{\alpha_1}L\right) - 1\right) \tag{45}$$

$$Q_{\text{inv}} = q\sqrt{\frac{2m_z KT}{q\pi\hbar^2}}exp\left[\frac{-\left(\left(\frac{E_g}{2} - q\phi(r = r_{\text{min}}, z = z_{\text{min}}) + \frac{\hbar^2}{2{r_c}^2}\left(\frac{1}{m_c}\right)(k_{0,1}r_c)^2 + \frac{\hbar^2}{2{r_c}^2}\left(\frac{1}{m_t}\right)(k_{0,1}r_c)^2\right)\right)}{V_T}\right] \tag{36}$$

$$a_7 = \frac{E_g}{2} + \frac{\hbar^2}{2{r_c}^2}\left(\frac{1}{m_c}\right)(k_{0,1}r_c)^2 + \frac{\hbar^2}{2{r_c}^2}\left(\frac{1}{m_t}\right)(k_{0,1}r_c)^2 + V_T \ln\left(\frac{Q_{\text{inv}}}{q\sqrt{\frac{2m_z V_T}{\pi\hbar^2}}}\right) + \frac{qN_a a_3}{\epsilon_{\text{si}}\alpha_1} \quad (46)$$

$$a_8 = \left[\left(2V_{\text{bi}}^2 + 2V_{\text{bi}}V_{\text{ds}}\right)(cosh\left(\sqrt{\alpha_1}L\right) - 1) - V_{\text{ds}}^2\right] + \left(2V_{\text{bi}} + V_{\text{ds}}\right)\frac{qN_a}{\epsilon_{\text{si}}\alpha_1}\left[(cosh\left(\sqrt{\alpha_1}L\right) - 1)\right] \quad (47)$$

Solving (39) gives the expression for threshold voltage V_{th}, as

$$V_{\text{th}} = V_{\text{fb}} + \left[\frac{-b + \sqrt{b^2 - 4ac}}{2a}\right] \quad (48)$$

where,

$$a = \left(a_1 a_2^2 - a_4^2\right) \quad (49)$$

$$b = \left(a_1^2 a_6 + 2a_2 a_7\right) \quad (50)$$

$$c = \left(a_1^2 a_8 - a_7^2\right) \quad (51)$$

IV. Results and Discussion

In this section, results obtained from the threshold voltage model are compared and verified with the numerical simulation results. Visual TCAD, a 3D device simulator from Cogenda Pvt. Ltd is used to carry out numerical simulations of the device. Density gradient quantum model, which is calibrated to match Poisson- Schrödinger solver, for the carrier transport incorporating quantization effect is used [21]. In order to account for concentration of inactive impurity atoms at low temperature, incomplete ionization is activated in numerical simulation.

Lombardi surface mobility model is considered for doping dependent bulk mobility, mobility degradation due to acoustic phonon scattering, and mobility degradation due to surface roughness scattering. Fermi-carrier statistics along with impact ionization of carrier under high lateral electric field are also considered for simulation.

Following the method of constant current for threshold voltage determination, V_{th} is extracted from the drain current-gate voltage curve by selecting the gate voltage at drain current value $I_{\text{d}} = \frac{W}{L} \times 10^{-7}$A, where, L is channel length and W is the effective width of the channel [11].

Fig. 5 shows the variation of inversion charge (Q_{inv}) along the tube thickness at channel length 20 nm, the gate and drain voltages are kept constant at 0.4 V and 0.1 V respectively. From the figure it is clear that the inversion charge has maxima at the centre of channel leading to the full volume inversion in DGAA MOSFET.

Fig. 6 represents the variation of threshold voltage V_{th} as a function of channel length with varying channel thickness t_{si}. It is evident from the figure that the threshold voltage increases with decrease in channel thickness at a fixed channel length. This may partially be attributed to increase in energy quantization in channel region with decrease in channel thickness t_{si}.

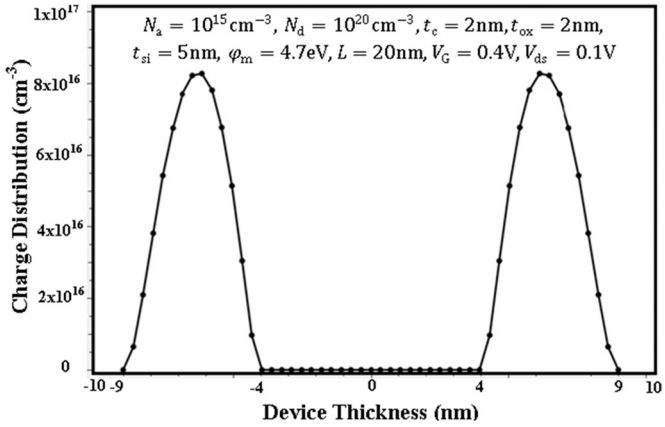

Fig. 5. Variation of charge distribution against device thickness at virtual cathode point.

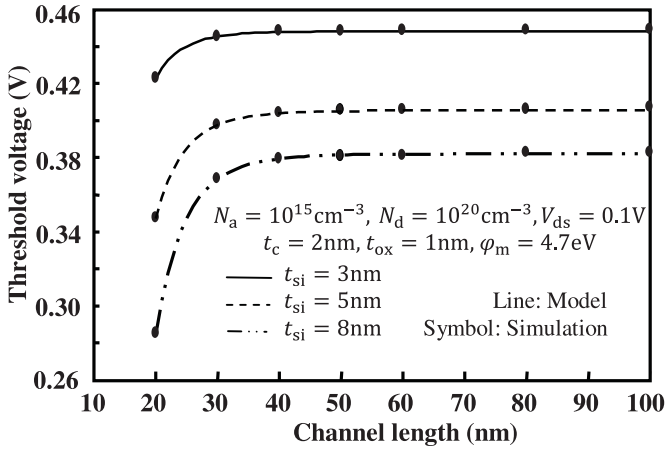

Fig. 6. Variation of Threshold voltage (V) against channel length for different values of channel thickness.

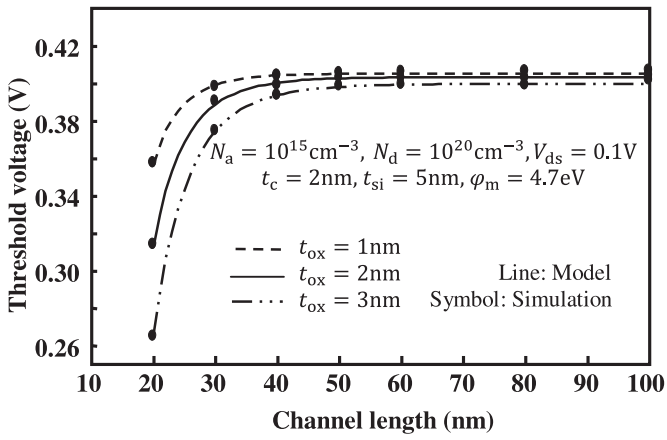

Fig. 7. Variation of Threshold voltage (V) against channel length for different values of oxide thickness.

In Fig. 7, the variation of threshold voltage V_{th} at different channel length with varying oxide thickness t_{ox} is plotted. The effective inner and outer oxide thickness expand with increase in t_{ox} resulting into reduction in gate control over the channel region. Thus the threshold voltage of the device undershoots and device turns ON at lower gate bias voltage.

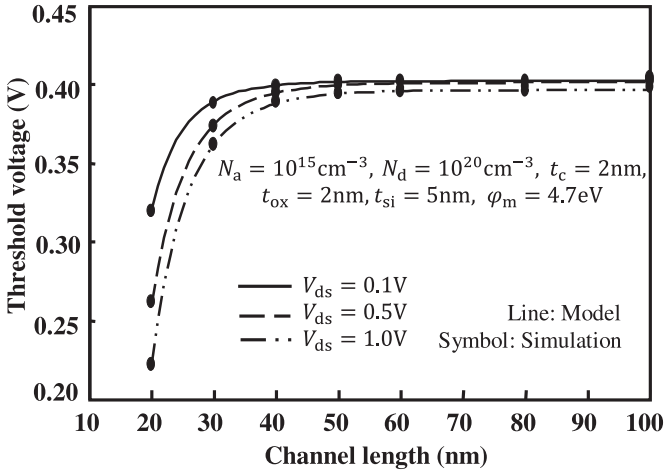

Fig. 8. Variation of Threshold voltage (V) against channel length for different values of drain voltage.

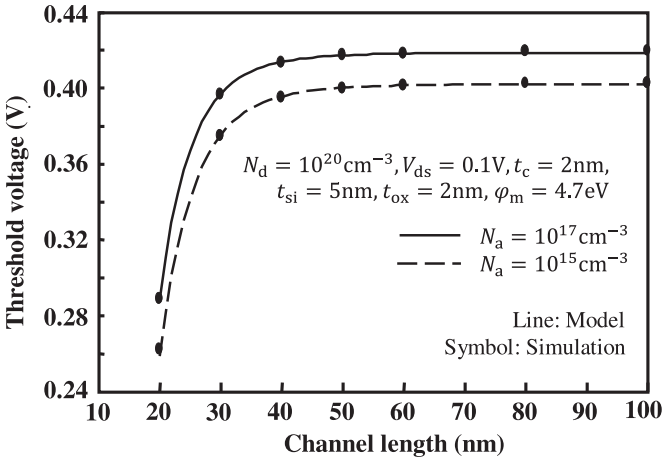

Fig. 9. Variation of Threshold voltage (V) against channel length for different values of channel doping concentration.

Figs. 8 and 9 show the variation of threshold voltage at different channel length with varying drain voltage V_{ds} and doping N_a of channel respectively. The threshold voltage can be observed decreasing with increase in drain bias whereas it increases corresponding to increase in doping of channel region. The positive shift of threshold voltage on increasing doping from $N_a = 10^{15}$atoms cm^{-3} to $N_a = 10^{17}$ atoms cm^{-3} is due to the mobility degradation from acoustic phonon scattering and surface roughness scattering.

The DIBL for an ultra-scaled short channel DGAA MOSFET may be defined as [22]

$$DIBL = \frac{(V_{th})_{V_{ds}=0.1v} - (V_{th})_{V_{ds}=1v}}{(V_{ds} = 1v) - (V_{ds} = 0.1v)} \tag{52}$$

Fig. 10 shows the DIBL variation against the channel length for different channel film thickness t_{si}. It is noticed that the DIBL is negligible for longer channel length above 40 nm, but is significant for smaller channel lengths. The device with thicker channel film suffers more from DIBL effects. This may be due to weak gate channel coupling which let the drain to enhance the control over channel charges.

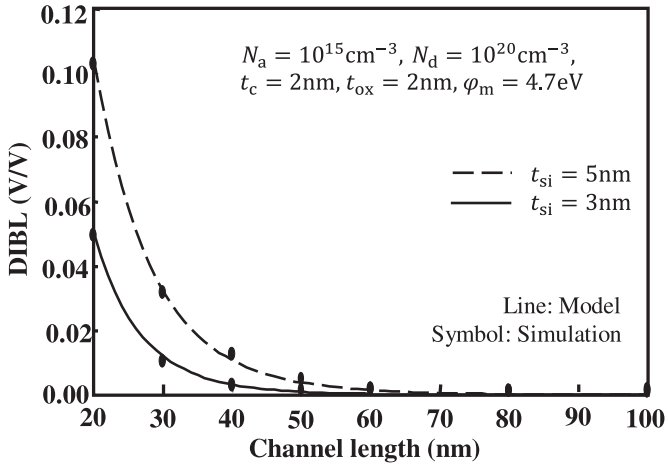

Fig. 10. Variation of DIBL (V/V) against channel length for different values of channel thickness.

It is worth mentioning that the threshold voltage model of (48) is simple and physical in nature. The present model is suitable for ultra-thin DGAA MOS devices as it incorporates the quantum confinement induced effects. The model accurately predicts the threshold voltage of the device even if the channel is as thin as 3nm and channel length is as short as 20 nm. Moreover, the model may also predict other short-channel effects like threshold voltage roll-off and DIBL in DGAA MOSFETs.

V. Conclusion

A quantum threshold voltage model for the DGAA MOSFET has been developed by solving the decoupled Schrödinger's and Poisson's equations. Simple equations for the wave-function and energy quantization in channel of DGAA MOSFET have been formulated. The effects of the device parameters like the channel thickness, oxide thickness, doping etc. on threshold voltage and DIBL have been extensively studied and verified. Proposed model results have found to be in good agreement with the numerical simulation results obtained from 3D device simulator, Visual TCAD of Cogenda Int. [21].

References

[1] International technology roadmap for semiconductors (ITRS). [Online]. Available: http://www.semiconductors.org/clientuploads/Research_Technology/ITRS/2015/0_2015%20ITRS%202.0%20Executive%20Report%20(1).pdf

[2] S. M. Sze, *Semiconductor Devices: Physics and Technology*, 2nd ed. New Delhi, India: Wiley, 2009, ch. 6, pp. 170–218.

[3] H. M. Fahad and M. M. Hussain, "Are nanotube architectures more advantageous than nanowire architectures for field effect transistors?" *Nature Sci. Rep.*, vol. 2, no. 475, pp. 1–7, Jun. 2012.

[4] J. P. Colinge, "The new generation of SOI MOSFETs," *Romanian J. Inf. Sci. Technol.*, vol. 11, no. 1, pp. 3–15, Nov. 2008.

[5] J. Dura *et al.*, "Analytical model of drain current in nanowire MOSFETs including quantum confinement, band structure effects and quasi-ballistic transport: device to circuit performances analysis," in *Proc. Int. Conf. Simul. Semicond. Process. Devices*, Osaka, Japan, 2011, pp. 43–46.

[6] J. L. Autran, K. Nehari, and D. Munteanu, "Compact modeling of the threshold voltage in silicon nanowire MOSFET including 2D-quantum confinement effects," *Mol. Simul.*, vol. 31, no. 12, pp. 839–843, Oct. 2005.

[7] Y. B. Kim, "Challenges for nanoscale MOSFETs and emerging nanoelectronics," *Trans. Elect. Electron. Mater.*, vol. 11, no. 3, pp. 93–105, Jun. 2010.

[8] D. Tekleab, "Device performance of silicon nanotube field effect transistors," *IEEE Electron. Device Lett.*, vol. 35, no. 5, pp. 506–508, May 2014.
[9] D. Tekleab, H. H. Tran, J. W. Sleight, and D. C hidambarrao, "Silicon nanotube MOSFET," U.S. Patent 20120217468 A1, Aug. 30, 2012.
[10] H. M. Fahad, C. E. Smith, J. P. Rojas, and M. M. Hussain, "Silicon nanotube field effect transistor with core-shell gate stacks for enhanced high-performance operation and area scaling benefits," *Nano Lett*., vol. 11, no. 10, pp. 4393–4399, Sep. 2011.
[11] P. K. Tiwari, V. R. Samoju, T. Sunkara, S. Dubey, and S. Jit,"Analytical modeling of threshold voltage for symmetrical silicon nano-tube field-effect-transistors (Si-NT FETs)," *J. Comput. Electron.*, vol. 15, no. 2, pp. 516–524, Apr. 2016.
[12] V. P. Trivedi and J. G. Fossum, "Quantum–mechanical effects on the threshold voltage of undoped double-gate MOSFETs," *IEEE Electron. Device Lett.*, vol. 26, no. 8, pp. 579–582, Aug. 2005.
[13] C. W. David, "The particle in a box (and in a circular box)," Digital Commons@UConn, no. 12, Aug. 2006. [Online]. Available: http://digitalcommons.uconn.edu/cgi/viewcontent.cgi?article=1013&context=chem_educ
[14] J. Gravesen, M. Willatzen, and L. Voon, "Schrödinger problems for surfaces of revolution—The finite cylinder as a test example," *J. Math. Phys.*, vol. 46, no. 1, Jan 2005, Art. no. 012107.
[15] M. Masale, N. C. Constantinou, and D. R. Tilley, "Single electron subbands of a hollow cylinder in an axial magnetic field," *Phys. Rev. B*, vol. 46, no. 23, Jul. 1992, Art. no. 15432.
[16] E. Gnani, S. Reggiani, M. Rudan, and G. Baccarani, "A new approach to the self-consistent solution of the Schrodinger-Poisson equations in nanowire MOSFETs," in *Proc. 34th Eur. Solid-State Circuits Conf.*, Belgium, 2004, pp. 177–180.
[17] J. Dura *et al.*, "Nanowires: Promising candidates for electrostatic control in future nanoelectronic devices," in *Electrostatics*. Rijeka, Croatia: In Tech, 2012, ch. 5, pp. 113–136. [Online]. Available: http://cdn.intechopen.com/pdfs-wm/31997.pdf
[18] E. Gnani, S. Reggiani, M. Rudan, and G. Baccarani, "Effects of the band-structure modification in silicon nanowires with small diameters," in *Proc. Solid State Device Res. Conf.*, 2006, pp. 170–173.
[19] M. Baldo, "Introduction to nanoelectronics," MIT OpenCourseWare Publication, May 2011, [Online]. Available: https://ocw.mit.edu/courses/electrical-engineering-and-computer-science/6-701-introduction-to-nanoelectronics-spring-2010/readings/MIT6_701S10_notes.pdf
[20] P. R. Kumar and S. Mahapatra, "Quantum threshold voltage modeling of short channel quad gate silicon nanowire transistor," *IEEE Trans. Nanotechnol.*, vol. 10, no. 1, pp. 121–128, Jan.2011.
[21] CogendaPte, Singapore, Genius, 3-D *Device Simulator, Version 1.9.0, Reference Manual*, 2008.
[22] Y. Tsividis, *Operational Modeling of the MOS Transistor*, 2nd ed. New York, NY, USA: McGraw-Hill, 1999.

Arun Kumar was born in Patna, India, in 1992. He received the B.E. degree in electronics and communication engineering from the RTM Nagpur University, Nagpur, India, in 2014. He is currently working toward the Ph.D. degree in the Department of Electrical Engineering, Indian Institute of Technology Patna, Patna.

His research interests include nanoscale device modeling and computational nanoelectronics. He received the Junior research fellowship from the Council of Scientific and Industrial Research, India.

Shiv Bhushan was born in Muzaffarpur, India, in 1986. He received the B.E. degree in electronics and telecommunication engineering from North Maharashtra University, Jalgaon, India, in 2009, and the M.Tech. degree in VLSI and embedded system from the National Institute of Technology, Rourkela, India, in 2013.

He is currently a Ph.D. Research Scholar in the Department of Electrical Engineering, Indian Institute of Technology Patna, Patna, India. His current research interests include semiconductor device modeling and simulation.

Pramod Kumar Tiwari (M'13) was born in Deoria, India, in 1981. He received the B.E. degree in electronics and telecommunication from Chaudhary Charan Singh University, Meerut, India, in 2002, the M.Tech. degree in electronics engineering from Aligarh Muslim University, Aligarh, India, in 2007, and the Ph.D. degree in microelectronics engineering from the Indian Institute of Technology, Banaras Hindu University, Varanasi, India, in 2012.

From 2011 to 2015, he was an Assistant Professor at the Department of Electronics and Communication Engineering, National Institute of Technology, Rourkela, India. Since January 2016, he has been an Assistant Professor in the Department of Electrical Engineering, Indian Institute of Technology Patna, India. He has published more than 80 papers in international journals and conferences in the area of semiconductor device modeling. His research interests include computational nanoelectronics, device modeling, and simulation.